

1 **m-NLP inference models using simulation and**
2 **regression techniques**

3 **Guangdong Liu¹, Sigvald Marholm^{2,3}, Anders J. Eklund⁴, Lasse Clausen²,**
4 **Richard Marchand¹**

5 ¹Department of Physics, University of Alberta, Edmonton, AB, Canada

6 ²Department of Physics, University of Oslo, Oslo, Norway

7 ³Department of Computational Materials Processing, Institute for Energy Technology, Kjeller, Norway

8 ⁴Materials Physics Oslo, SINTEF Industry, Oslo, Norway

9 **Key Points:**

- 10 • 3-D kinetic PIC simulations are used to simulate currents collected by m-NLP in
11 order to create a synthetic solution library
- 12 • Models to infer physical parameters from m-NLP measurements are constructed
13 and assessed on the basis of synthetic and in situ data sets
- 14 • Promising new approaches are identified to better analyze m-NLP measurements,
15 for future low and mid Earth orbit missions

Corresponding author: Guangdong Liu, guangdon@ualberta.ca

Abstract

Current inference techniques for processing multi-needle Langmuir Probe (m-NLP) data are often based on adaptations of the Orbital Motion-Limited (OML) theory which relies on several simplifying assumptions. Some of these assumptions, however, are typically not well satisfied in actual experimental conditions, thus leading to uncontrolled uncertainties in inferred plasma parameters. In order to remedy this difficulty, three-dimensional kinetic particle in cell simulations are used to construct a synthetic data set, which is used to compare and assess different m-NLP inference techniques. Using the synthetic data set, regression-based models capable of inferring electron density and satellite potentials from 4-tuples of currents collected with fixed-bias needle probes similar to those on the NorSat-1 satellite, are trained and validated. The regression techniques presented enable excellent inferences of the plasma density, and floating potentials. The new inference approaches presented are applied to NorSat-1 data, and compared with existing state of art inference techniques.

1 Introduction

Langmuir probes are widely used to characterize space plasma and laboratory plasma. A variety of Langmuir probe geometries are being used, such as spherical (Bhattarai & Mishra, 2017), cylindrical (Hoang, Clausen, et al., 2018), and planar probes (Lira et al., 2019; Johnson & Holmes, 1990; Sheridan, 2010). Probes can be operated in sweep mode (Lebreton et al., 2006), harmonic mode (Rudakov et al., 2001), or fixed biased mode (Jacobsen et al., 2010), for different types of missions and measurements. Despite operational differences, all Langmuir probes consist of conductors exposed to plasma to collect current as a function of bias voltage. A common approach to infer plasma parameters from Langmuir probes is to sweep the bias voltage and produce a current-voltage characteristic, which can be analyzed using theories such as the Orbital Motion-Limited (OML) (Mott-Smith & Langmuir, 1926) theory, the Allen-Boyd-Reynolds (ABR) theory (Allen et al., 1957; Chen, 1965, 2003), and the Bernstein-Rabinowitz-Laframboise (BRL) theory (Bernstein & Rabinowitz, 1959; Laframboise, 1966) to obtain plasma parameters such as density, temperature, and satellite floating potential. The temporal and, on a satellite, the spatial resolution of Langmuir probe measurements are determined by the sweep time, which varies based on the mission's scientific need and available resources. Considering the orbital speed to be around 7500 m/s for a satellite in low Earth orbit (LEO), the spatial resolution of sweep bias Langmuir probe can vary from tens of meters, to kilometers, depending on the sweep frequency. In order to study the formation of density irregularities that scale from meters to tens of kilometers at high and low latitudes, a sampling frequency of near 1 kHz is required (Hoang, Røed, et al., 2018; Jacobsen et al., 2010). A solution, proposed by Jacobsen is to use multiple fixed biased needle probes (m-NLPs) to sample plasma simultaneously at different bias potentials in the electron saturation region (Jacobsen et al., 2010). This approach would eliminate the need for sweeping the bias voltage, and greatly increase the sampling rate of the instrument.

The first inference models for m-NLPs relied on the OML approximation, from which the current I_e collected by a needle probe in the electron saturation region is written as:

$$I_e = -n_e e A \frac{2}{\sqrt{\pi}} \sqrt{\frac{kT_e}{2\pi m_e}} \left(1 + \frac{e(V_f + V_b)}{kT_e} \right)^\beta, \quad (1)$$

where n_e is the electron density, A is the probe surface area, e is the elementary charge, k is Boltzmann's constant, T_e is the electron temperature, V_f is the satellite floating potential, V_b is the bias potential of the probe with respect to the satellite, and β is a parameter related to probe geometry, density, and temperature (Marholm & Marchand, 2020; Hoang, Røed, et al., 2018). Several assumptions were made in the derivation of this inference equation; such as the probe length must be much larger than the Debye length, and the plasma is non-drifting. If these assumptions are valid, then $\beta = 0.5$, and as first

66 suggested by Jacobsen, a set of m-NLPs can be used to infer the electron density inde-
 67 pendently of the temperature (Jacobsen et al., 2010). For a satellite in near-Earth or-
 68 bit at altitudes ranging from 550 km to 650 km, we can expect a Debye length of around
 69 2-50 mm, and an orbital speed of around 7500 m/s. A common length for m-NLP in-
 70 strument used on small satellites is ~ 25 mm (Bekkeng et al., 2010; Hoang, Clausen,
 71 et al., 2018; Hoang et al., 2019), which is often comparable to, and sometimes smaller
 72 than the Debye length. In lower Earth orbit, ion thermal speeds are usually less than
 73 the orbital speed, while electron thermal speeds are usually higher than the orbital speed.
 74 Thus, the orbital speed is expected to mainly affect ion saturation region currents for
 75 Langmuir probes. However, electrons can only penetrate the ion rarefied wake region be-
 76 hind the probe as much as ambipolar diffusion permits (Barjatya et al., 2009). As a re-
 77 sult, electron saturation currents are also influenced by an orbital speed. One consequence
 78 is that the $\beta = 0.5$ assumption does not hold in Eq. 1, and a better approximation for
 79 the current is obtained with β values between 0.5 and 1. For example, in a hot filament-
 80 generated plasma experiment, Sudit and Woods showed that β can reach 0.75 for a ra-
 81 tio between the Debye length and the probe length in the range of 1 to 3. For larger De-
 82 bye lengths, they also observed an expansion of the probe sheath from a cylindrical shape
 83 into a spherical shape (Sudit & Woods, 1994). Ergun and co-workers showed that with
 84 a ram speed of 4300 m/s in their simulations, the needle probe current is better approx-
 85 imated with Eq. 1 using a β value of 0.67 instead of 0.55 calculated in a stationary plasma
 86 (Ergun et al., 2021). In the ICI-2 sounding rocket experiment, β calculated from three
 87 25 mm m-NLPs varied between 0.3 to 0.7 at altitudes ranging from 150 to 300 km (Hoang,
 88 Røed, et al., 2018). Simulation results by Marholm et al. showed that even a 50 mm probe
 89 at rest can be characterized by a $\beta \sim 0.8$ (Marholm et al., 2019), in disagreement with
 90 the OML theory. In practice, needle probes are mounted on electrically isolated and equipo-
 91 tential guards in order to attenuate end effects on the side to which it is attached. The
 92 distribution of the current collected per unit length is nonetheless not uniform along the
 93 probe, as more current is collected near the end opposite to the guard. A study by Marholm
 94 & Marchand showed that for a cylindrical probe length that is 10 times the Debye length,
 95 β is approximately 0.72. For a probe length that is 30 times the Debye length, β is ap-
 96 proximately 0.62, and with a guard, this number is reduced to 0.58 (Marholm & Marc-
 97 hand, 2020). Although this number approaches 0.5, 30 times the Debye length is a strin-
 98 gent requirement for OML to be valid, and it is hardly ever fulfilled in practice. Exper-
 99 imentally, Hoskinson and Hershkowitz showed that even with a probe length 50 times
 100 the Debye length, β is approximately 0.6, and the density inference based on an ideal
 101 $\beta = 0.5$ is 25 % too high (Hoskinson & Hershkowitz, 2006). Barjatya estimated that
 102 even a 10% error in β (to 0.55) can result in a 30 % or more relative error in the calcu-
 103 lated density based on the $\beta = 0.5$ assumption (Barjatya & Merritt, 2018). In what fol-
 104 lows, we find that densities estimated using Eq. 1 assuming $\beta = 0.5$ are about three
 105 times larger than the known values used as input in our simulations, as illustrated in sec-
 106 tion 3.1. This is consistent with findings in (Barjatya & Merritt, 2018; Guthrie et al.,
 107 2021), considering β calculated in our simulation is in the range of 0.75 to 1. Another
 108 approach proposed to account for the fact that β is generally different from 0.5, consists
 109 of determining the n_e , V_b , T_e and β , as adjustable parameters in nonlinear fits of mea-
 110 sured currents as a function of voltages. This lead to remarkable agreement with den-
 111 sity measured using a radio frequency impedance probe on the international space sta-
 112 tion (Barjatya et al., 2009, 2013; Debchoudhury et al., 2021). This method was origi-
 113 nally applied to a probe operated in sweep voltage mode, but it can be straightforwardly
 114 adapted to fixed bias m-NLP measurements (Barjatya et al., 2009; Barjatya & Merritt,
 115 2018; Hoang, Røed, et al., 2018).

116 In the following, we assess different techniques to infer plasma densities, and satel-
 117 lite potentials from fixed bias needle probe measurements based on synthetic data ob-
 118 tained from kinetic simulations. We also present a new method to interpret m-NLP mea-
 119 surements based on multivariate regression. Our kinetic simulation approach and the con-
 120 struction of a synthetic data set are presented in Sec. 2. In Sec. 3, regression models are

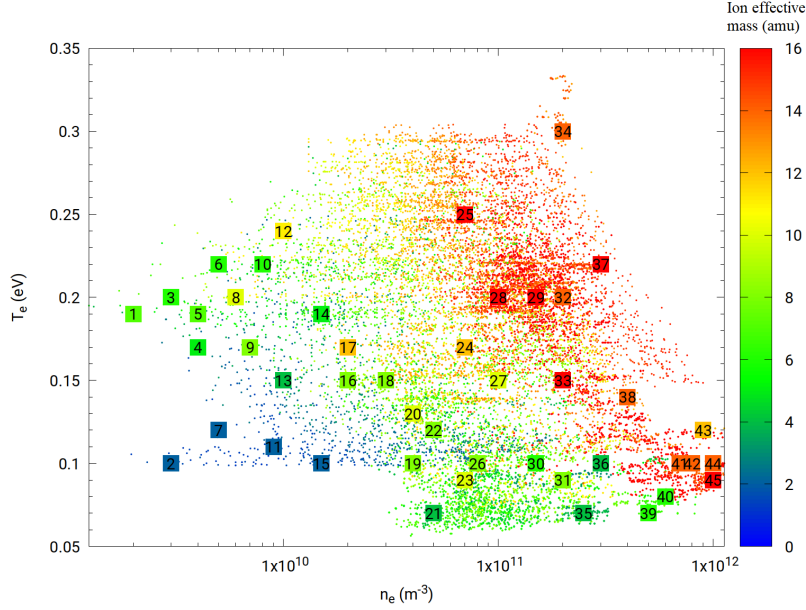


Figure 1. Scatter plot of plasma parameters obtained from the IRI model, corresponding to different latitudes, longitudes, altitudes, and times, as listed in Table 1. The x and y axes, and the color bar refer respectively, to the electron density, electron temperature, and the ion effective mass. Numbered squares identify the set of parameters used in the kinetic simulations.

121 trained using synthetic data sets, and they are assessed using distinct validation sets.
 122 In Sec. 4, the same models are applied to NorSat-1 data, to infer densities and satellite
 123 potentials from in situ measured currents. Section 5 summarizes our findings and presents
 124 some concluding remarks.

125 2 Methodology

126 In this section, we briefly describe our kinetic simulation approach, and how it is
 127 used to construct synthetic data sets used to train and validate inference models, using
 128 two regression techniques.

129 2.1 Kinetic simulations

130 The space plasma parameters considered in our simulations are selected so as to
 131 be representative of conditions expected for a satellite in low Earth orbit at altitudes rang-
 132 ing between 550 and 650 km. This is done by sampling ionospheric plasma parameters
 133 using the International Reference Ionosphere (IRI) (Bilitza et al., 2014) model in a broad
 134 range of latitudes, longitudes, altitudes, and times as shown in Fig. 1. The ranges con-
 135 sidered for these parameters are summarized in Tab. 1. Forty-five sets of plasma param-
 136 eters approximately evenly distributed in this parameter space are selected as input in
 137 simulations, as shown in numbered squares in Fig. 1. The three-dimensional PIC code
 138 PTetra (Marchand, 2012; Marchand & Lira, 2017) is used to simulate probe currents in
 139 this study. In the simulations, space is discretized using unstructured adaptive tetrahe-
 140 dral meshes (Frey & George, 2007; Geuzaine & Remacle, 2009). Poisson’s equation is
 141 solved at each time step using Saad’s GMRES sparse matrix solver (Saad, 2003) in order
 142 to calculate the electric field in the system. Then, electron and ion trajectories are
 143 calculated kinetically using their physical charges and masses self consistently. The mesh

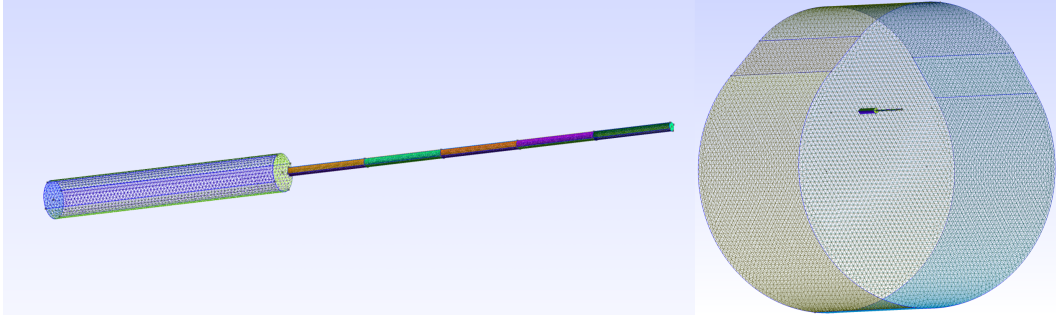


Figure 2. Illustration of a m-NLP geometry (left), and the simulation domain (right). The needle probe has a length of 25 mm and radius of 0.255 mm, with a guard of 15 mm in length and 1.1 mm in radius. The ram flow is from the top of the simulation domain and is assumed to be 7500 m/s.

144 for the m-NLP and the simulation domain illustrated in Fig. 2, is generated with GMSH
 145 (Geuzaine & Remacle, 2009). The needle probe used in the simulation has a length of
 146 25 mm and a diameter of 0.51 mm, as those on the NorSat-1. The needle probe is at-
 147 tached to a 15 mm long and 2.2 mm diameter guard which is biased to the same volt-
 148 age as the probe. The outer boundary of the simulation domain is closer to the probe
 149 on the ram side, and farther on the wake side, as shown in Fig. 2. The simulations are
 150 made using two different domain sizes depending on the Debye length of the plasma. For
 151 plasma density below $2 \times 10^{10} \text{ m}^{-3}$ corresponding to a Debye length of 1.9-7.2 cm, a
 152 larger domain is used. For plasma density above $2 \times 10^{10} \text{ m}^{-3}$, corresponding to a De-
 153 bye length of 0.2-2.2 cm, a smaller domain with finer resolution is used. The simulation
 154 size, the resolution, the number of tetrahedra, and the corresponding Debye length are
 155 summarized in Tab. 2. There is overlap between the two simulation domains for simu-
 156 lations with Debye lengths around 2 cm. No obvious difference was found in the simu-
 157 lated currents, indicating that simulation results from both domains are consistent in
 158 the transition range. Simulation results from both domains are included when training
 159 the regression models. All simulations are run initially with 100 million ions and elec-
 160 trons, but these numbers vary through a simulation, due to particles being collected, leav-
 161 ing, or entering the domain. In the simulations, the probe is segmented into five seg-
 162 ments of equal length, making it possible to estimate a rough distribution of the current
 163 along its length. The current used to build regression models is a sum of the currents of the
 164 five different segments. The orbital speed of the satellite is assumed to be fixed at 7500
 165 m/s in the simulations, with a direction perpendicular to the probe. For the voltages con-
 166 sidered, probes are expected to collect mainly electron currents. For simplicity, only two
 167 types of ions are considered in the simulation, O^+ and H^+ ions, and no magnetic field
 168 is accounted for in the simulation, which is justified by the fact that the Larmor radius
 169 of the electron considered is much larger than the radius of the probe.

170 2.2 Synthetic solution library

171 In order to assess the inference skill of a regression model, a cost function is de-
 172 fined with the following properties: i) it is positive definite, ii) it vanishes if model in-
 173 ferences agree exactly with known data in a data set, and iii) it increases as inferences
 174 deviate from actual data. The cost functions used in this work are: the root mean square
 175 error,

$$176 \text{RMS} = \sqrt{\frac{1}{N_{data}} \sum_{i=1}^{N_{data}} (Y_{mod_i} - Y_{data_i})^2}, \quad (2)$$

Table 1. Spatial and temporal parameters used to sample ionospheric plasma conditions in IRI, and the corresponding ranges in space plasma parameters.

Environment and plasma conditions	Parameter range
Years	1998 2001 2004 2009
Dates	Jan 4 Apr 4 Jul 4 Oct 4
Hours	0-24 with increment of 8 hours
Latitude	-90° - $+90^\circ$ with increment of 5°
Longitude	0° - -360° with increment of 30°
Altitude	550-650 km with increment of 50 km
Ion temperature	0.07-0.16 eV
Electron temperature	0.09-0.25 eV
Effective ion mass	2-16 amu
Density	$2 \times 10^9 - 1 \times 10^{12} \text{m}^{-3}$

Table 2. Parameters used in the two simulation domains are listed. The first two columns give the distances between the probe to the outer boundary on the ram side (D_{ram}), and the wake side (D_{wake}) respectively, followed by the simulation resolutions at the probe, guard, and the outer boundary. The number of tetrahedra used in the simulations is in the order of millions. The corresponding range in Debye lengths is also listed.

D_{ram}	D_{wake}	Probe resolution	Guard resolution	Boundary resolution	Tetrahedra	Debye length
3.5 cm	7 cm	51 μm	220 μm	2 mm	2.5 M	0.2-2.2 cm
30 cm	40 cm	51 μm	220 μm	1 cm	1.7 M	1.9-7.2 cm

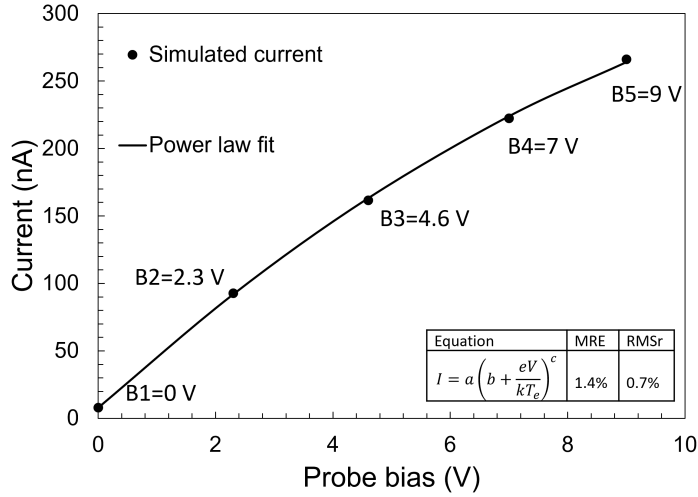


Figure 3. Comparison between calculated currents from PIC simulations, and fitted values using Eq. 6, assuming a density of $2 \times 10^{10} \text{m}^{-3}$, an effective mass of 8 amu, an electron and ion temperatures of 0.15 and 0.12 eV respectively, corresponding to point 16 in Fig. 1. The fitting errors in the figure are calculated over all 45 sets of plasma conditions using Eq. 3 and 5.

177 the root mean square relative error

$$178 \quad RMSr = \sqrt{\frac{1}{N_{data}} \sum_{i=1}^{N_{data}} \frac{(Y_{mod_i} - Y_{data_i})^2}{Y_{mod_i}^2}}, \quad (3)$$

179 the maximum absolute error

$$180 \quad MAE = \max \{|Y_{mod} - Y_{data}|\}, \quad (4)$$

181 and the maximum relative error

$$182 \quad MRE = \max \left\{ \left| \frac{Y_{mod} - Y_{data}}{Y_{mod}} \right| \right\}, \quad (5)$$

183 where Y_{data} and Y_{mod} represent respectively known and inferred plasma parameters, and
184 N_{data} is the total number of data points.

185 For each set of plasma conditions corresponding to a square in Fig. 1, 5 simula-
186 tions are made assuming 5 probe voltages with respect to background plasma, and the
187 simulated currents vs probe voltage are fitted analytically with:

$$188 \quad I = a \left(b + \frac{eV}{kT_e} \right)^c, \quad (6)$$

189 where a, b, and c are adjustable fitting parameters. The MRE calculated for all 45 fits
190 is 1.4%, and the RMSr is 0.7%, which shows excellent agreement with simulated collected
191 currents. A comparison between fitted and computed currents is shown in Fig. 3. The
192 NorSat-1 m-NLP probes fixed biases V_b are +10, +9, +8, and +6 V, and the probe volt-
193 age with respect to background plasma is given by the sum of the spacecraft floating po-
194 tential plus the probe bias $V = V_f + V_b$. In simulations, probe currents are calculated
195 for voltages with respect to background plasma in the range between 0 to 9 volts are con-
196 sidered as shown in Fig. 3. Considering the probe bias voltages V_b given above, probe
197 currents can be determined, corresponding to arbitrary floating potentials between -1
198 V and -6 V. A synthetic solution library is created for randomly distributed spacecraft
199 floating potentials in the range between -1 and -6 V with corresponding currents obtained
200 by interpolation using Eq. 6 with the fitting parameters computed for each of the 45 cases
201 considered. The result is a synthetic solution library consisting of four currents collected
202 by the four needle probes at the four different bias voltages, for 160 randomly distributed
203 spacecraft potentials in the range between -1 V to -6 V for each of the 45 sets of plasma
204 parameters. In each entry of the data set, these four currents are followed by the elec-
205 tron density, the spacecraft potential the electron and ion temperatures, and the ion ef-
206 fective mass as illustrated in Tab. 3. The resulting solution library consisting of $45 \times$
207 $160 = 7200$ entries is then used to construct a training set with 3600 randomly selected
208 nodes or entries, and a validation set with the remaining 3600 nodes. The cost functions
209 reported in what follows, used to assess the accuracy of inferences, are all calculated from
210 the validation data set unless stated otherwise.

211 **2.3 Multivariate regression**

212 The next step is to construct a multivariate regression model that maps the cur-
213 rents to the corresponding plasma conditions in the solution library. In a complex sys-
214 tem where the relation between independent variables and dependent variables cannot
215 readily be cast analytically, multivariate regressions based on machine learning techniques
216 are powerful alternatives to construct approximate inference models. In this approach,
217 the model must be capable of capturing the complex relationship between dependent and
218 independent variables. Once the model is trained using the training set, it can then be
219 used to make inferences for cases not included in the training data set. In this work, two
220 multivariate regression approaches are used to infer plasma parameters: the Radial Ba-
221 sis Function and Feedforward Neural Networks. The models are trained by optimizing

Table 3. Example entries of the synthetic data set, with currents I_1 , I_2 , I_3 , and I_4 calculated using Eq. 6, and V_b set to 10, 9, 8, and 6 V, respectively. The floating potential V_f is selected randomly in the range of -1 to -6 V, and the probe voltages with respect to background plasma are given by $V = V_b + V_f$. The coefficients, a, b and c are obtained from a nonlinear fit of the simulated currents using Eq. 6. The first and second entries correspond respectively to points 16 and 21 in Fig. 1.

$I_1(nA)$	$I_2(nA)$	$I_3(nA)$	$I_4(nA)$	$V_f(V)$	$n_e(m^{-3})$	$T_e(eV)$	$T_i(eV)$	$m_{eff}(amu)$
233	208	183	129	-2.50	2×10^{10}	0.15	0.12	8
596	533	467	323	-2.93	5×10^{10}	0.07	0.07	4

222 their cost function on the training data set, and then applied to the validation data set
223 to calculate the validation cost function without further optimization. The use of a val-
224 idation set is to avoid ‘‘overfitting’’ because there are certain limitations on the refine-
225 ment of a model on a training set, such that further improvement of model inference skill
226 in the training set will worsen the model inference skill in the validation set. A good model
227 is one with the right level of training so as to provide the best inference skill in the val-
228 idation set.

2.3.1 Radial basis function

229 Radial basis function (RBF) multivariate regression is a simple and robust tool used
230 in many previous studies to infer space plasma parameters using a variety of instruments
231 with promising results (Liu & Marchand, 2021; Olowookere & Marchand, 2021; Chalaturnyk
232 & Marchand, 2019; Guthrie et al., 2021). A general expression for RBF regression for
233 a set of independent n-tuples \bar{X} and corresponding dependent variable Y is given by:
234

$$235 \quad Y = \sum_{i=1}^N a_i G(|\bar{X} - \bar{X}_i|). \quad (7)$$

236 In general, the dependent variable Y can also be a tuple, but for simplicity, and with-
237 out loss of generality, we limit our attention to scalar dependent variables. In Eq. 7, the
238 \bar{X}_i represents the N centers, G is the interpolating function, and the a_i are fitting col-
239 location coefficients which can be determined by requiring collocation at the centers; that
240 is, by solving the system of linear equations

$$241 \quad \sum_{i=1}^N a_i G(|\bar{X}_k - \bar{X}_i|) = Y_k \quad (8)$$

242 for $k = 1, \dots, N$. Here, the dependent variable Y corresponds to the physical param-
243 eter to be inferred, and the independent variable \bar{X} is a 4-tuple corresponding to the cur-
244 rents or the normalized currents from the m-NLPs depending on which physical param-
245 eters are being inferred. There are different ways to distribute the centers in RBF re-
246 gression. One straightforward approach is to select centers from the training data set,
247 and evaluate the cost function over the entire training data set for all possible combi-
248 nations of centers, then select the model which yields the optimal cost function. For this
249 approach, the number of combinations required for \mathcal{N} data points and N centers is given
250 by

$$251 \quad \binom{\mathcal{N}}{N} = \frac{\mathcal{N}!}{N!(\mathcal{N} - N)!}. \quad (9)$$

252 This, of course, can be prohibitively large and time-consuming for a large training data
253 set or using a large number of centers. An alternative strategy is to successively train

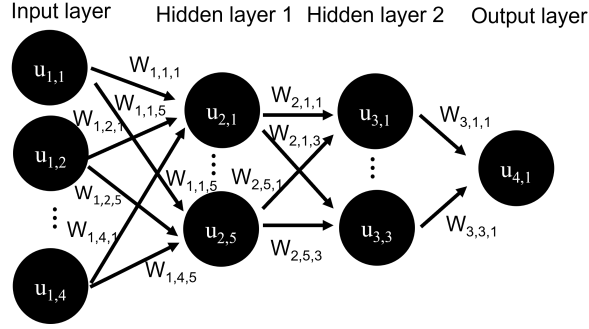


Figure 4. Schematic of a feedforward neural network.

254 models with randomly selected small subsets of the entire training data set using the straight-
 255 forward approach, while calculating the cost function on the full training set, and then
 256 carrying the optimal centers from one iteration to the next. This “center-evolving strat-
 257 egy” is very efficient in finding near-optimal centers for large training data sets and has
 258 proven to be as accurate as the straightforward extensive approach. The RBF models
 259 here follow this procedure. Different G functions and cost functions are tested, and only
 260 the models that yield optimal results are reported in this paper.

261 **2.3.2 Feedforward neural network**

262 The second multivariate regression approach is a Feedforward neural network as
 263 illustrated in Fig. 4. This consists of an input layer, hidden layers, and an output layer.
 264 Each node j in a given layer i in the network is assigned a value $u_{i,j}$, and the node in
 265 the next layer $i+1$ are “fed” from numerical values from the nodes in the previous layer
 266 according to

$$267 \quad u_{i+1,k} = f \left(\sum_{j=1}^{n_i} w_{i,j,k} u_{i,j} + b_{i,k} \right), \quad (10)$$

268 where $w_{i,j,k}$ are weight factors, $b_{i,j}$ are bias terms, and f is a nonlinear activation func-
 269 tion (Goodfellow et al., 2016). In this work, the input layer neurons contain the four-
 270 needle probe currents or normalized currents depending on the physical parameter to
 271 be inferred, whereas the output layer contains one physical parameter. The number of
 272 hidden layers and the number of neurons in the hidden layers are adjusted to fit the spe-
 273 cific problem, and attain good inference skills. The Feedforward neural network is built
 274 using TensorFlow (Abadi et al., 2016) with Adam optimizer (Kingma & Ba, 2015), and
 275 using the ReLU activation function defined as $f(x) = \max(0, x)$. The input variables
 276 are normalized using the `preprocessing.normalization` TensorFlow built-in function
 277 which normalizes the data to have a zero mean and unit variance. The structure of the
 278 network will be described later when presenting model inferences.

279 **3 Assessment with synthetic data**

280 In this section, we assess our models using synthetic data, which allows us to check
 281 the accuracy, and quantify uncertainties in our inferences. A consistency check strategy
 282 is also introduced to further assess the applicability of our models.

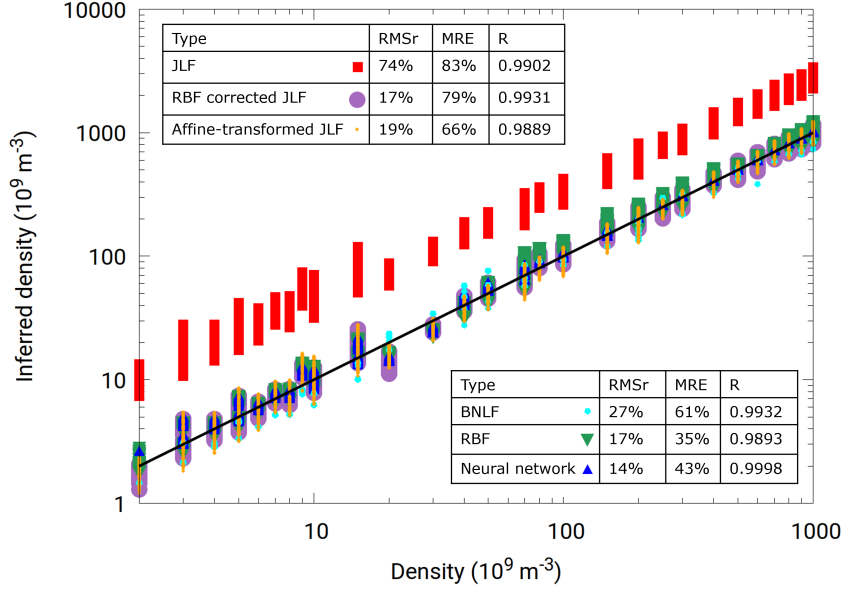


Figure 5. Correlation plot for the density inferences made with different techniques applied to our synthetic validation set. The Pearson correlation coefficient R is calculated using the inferred densities and the density used in the simulation. Black line represent idealized perfect correlation line.

283

3.1 Density inference

284

The density can be inferred using Eq. 1 which can be rewritten as

$$\frac{n_e}{T_e^{\beta-\frac{1}{2}}} = \sqrt{\frac{\pi^2 m_e}{2A^2 e^3}} \left(\frac{I_1^{\frac{1}{\beta}} - I_2^{\frac{1}{\beta}}}{V_1 - V_2} \right)^\beta. \quad (11)$$

286

In this equation, subscripts 1 and 2 indicate different probes. A special case of this equation was first proposed by Jacobsen, assuming an infinitely long probe, for which $\beta = 0.5$, resulting in

288

$$n_e = \sqrt{\frac{\pi^2 m_e}{2A^2 e^3}} \sqrt{\frac{I_1^2 - I_2^2}{V_1 - V_2}}, \quad (12)$$

289

290 which gives an expression for the electron density, independently of the temperature (Jacobsen
 291 et al., 2010). With currents from more than two probes, the density can be calculated
 292 from the slope of the current squared as a function of the bias voltage from a linear least-
 293 square fit of all probes (Jacobsen et al., 2010). This will be referred as the “Jacobsen lin-
 294 ear fit” (JLF) approach. On the other hand, the $\beta = 0.5$ assumption requires that the
 295 needle probe be very long compared to the Debye length, which is in general not satis-
 296 fied for NorSat-1 satellite. As a consequence, when this method is applied to the solu-
 297 tion library, the inferred density is typically three times larger than the actual density
 298 as shown with red boxes in Fig 5. Despite this offset, the high Pearson correlation co-
 299 efficient R shows that inferences made with this method can be significantly improved
 300 with a simple affine transformation. The best results are obtained by applying an affine
 301 transformation to the log of the JLF inferred density as in:

302

$$\ln(n'_e) = a \ln(n_e) + b. \quad (13)$$

303

In this equation, the density n_e is first obtained using the JLF method, then an affine
 304 transformation is used to calculate the inferred density n'_e . The affine transformation co-

305 efficient coefficients a and b are obtained from a least-squares fit of the log of these densities, to those
 306 in the training data set. The fitting coefficients in this case, $a = 1.13261$ and $b = -4.82735$,
 307 are then used to perform an affine transformation on the validation data set, leading to
 308 a significant improvement in RMSr from 74% to 19%, and in MRE from 83% to 66% com-
 309 pared to densities inferred from the JLF approach, as shown in Fig 5. RBF regression
 310 can also be used to correct JLF density. This is done by using RBF to approximate the
 311 discrepancy between the densities used in the simulations and the ones inferred with JLF.
 312 This correction is then used to improve the accuracy of the inferred density obtained with
 313 JLF method. Using the four currents as input variable \bar{X} , by minimizing the MRE, us-
 314 ing $G(x) = |x|$, and using 5 centers, the RBF corrected JLF density yields an RMSr
 315 of 17 % and a MRE of 79%. The cost functions of the two methods are comparable, but
 316 an obvious advantage of using an affine transformation is its simplicity.

317 Barjatya’s nonlinear least square fit method is also assessed using our synthetic data
 318 set. The original method was applied to sweep mode measurements, to obtain the elec-
 319 tron temperature and the satellite potential from currents in the ion saturation region
 320 and electron retardation region currents, before fitting the density and β from the elec-
 321 tron saturation region (Barjatya et al., 2009). This is however not possible with fixed
 322 bias probe measurements considered here. On NorSat-1, four currents are measured si-
 323 multaneously, by four probes at different fixed bias voltages, all in the electron satura-
 324 tion region. A similar approach can nonetheless be applied in our case, using a nonlin-
 325 ear fit to the currents, with the density, the electron temperature, the satellite poten-
 326 tial, and β , as fitting parameters. As shown by Barjatya and Merritt (Barjatya & Mer-
 327 ritt, 2018), however, it is difficult to infer the temperature using this approach, owing
 328 to the weak dependence of collected currents on the electron temperature (see Eq. 11).
 329 A solution, proposed in (Barjatya & Merritt, 2018; Hoang, Røed, et al., 2018), then con-
 330 sists of estimating the electron temperature from other measurements, or from the IRI
 331 model, and perform the fit for the remaining three parameters. This simplification is jus-
 332 tified by the fact that, following this procedure, a 50% error in the temperature, still pro-
 333 duces acceptable results for the other parameters (Barjatya & Merritt, 2018). Thus in
 334 this study, we assume a fixed electron temperature (~ 2000 K), which is in the middle
 335 of the temperature range considered in the simulations, and fit 4-tuples of currents us-
 336 ing potentials, densities, and β values as fitting parameters. This will be referred as the
 337 “Barjatya nonlinear fit” (BNLF) approach. The Python 3 `differential.evolution` pack-
 338 age is used to do the nonlinear fit with an evolution strategy of ‘best2exp’, with a tol-
 339 erance of `tol=0.001`. In the fits, the upper and lower bounds for the density, the poten-
 340 tial and the β value are 1×10^9 to 1×10^{12} m^{-3} , -6 to -1 V, and 0.5 to 1, respectively.
 341 The potential lower bound of -6 V is needed to ensure that the values under exponent
 342 in Eq. 1 are positive. We obtain 3600 fits for each of the 3600 entries of four currents
 343 in our validation data set. The fit minimizes RMSr as the cost function, and the over-
 344 all RMSr calculated using Eq. 3 for the 3600×4 currents is 0.02 %, and only 0.26% of
 345 the points have relative errors larger than 1%. The resulting density inferences have an
 346 RMSr of 27 % and a MRE of 61 %, which is better than the densities inferred from the
 347 JLF approach, but less accurate than the affine-transformed JLF density. The β values
 348 calculated are in the range of 0.75 to 1. The inferred potential using this method is dis-
 349 cussed in the next section together with other methods. With only four fitting points,
 350 the fit can fail into local minimums instead of the global minimum, thus, the tolerance
 351 of the fit must be small. As a result, the nonlinear fits tend to be somewhat time-consuming,
 352 with each fit requiring approximately 1 second using an AMD 5800x processor. In com-
 353 parison, linear fits of the currents square, followed by an affine transformation of the log
 354 of the inferred density can be done using fixed formulas, and thus are considerably faster
 355 than a nonlinear fit. Regression methods such as RBF or neural network are also numer-
 356 ically very efficient, considering they involve simple arithmetic expressions with pre-calculated
 357 coefficients.

358 Direct RBF regression can be applied to infer density using the four currents as
 359 input variables. When constructing an RBF model with $G(x) = |x|$, minimizing MRE,

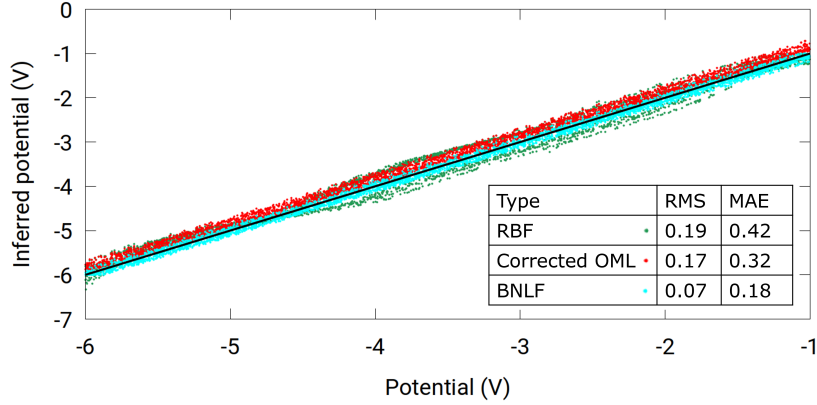


Figure 6. Correlation plot obtained for satellite potential inferred with RBF and OML techniques.

360 and using 6 centers, the RMSr and MRE calculated on the validation data set are 17%
 361 and 35%, respectively. Using a neural network with 4 nodes in the input layer, 14 nodes
 362 and 12 nodes in two hidden layers, and 1 node in the output layer, results in a 14% RMSr
 363 and 43% MRE for the inferred densities. This is calculated using TensorFlow with ADAM
 364 optimizer with a learning rate of 0.005 and an RMSr as a cost function. The input layer
 365 is normalized to have a zero mean and unit variance, while the output layer is normal-
 366 ized by dividing the largest density. The densities calculated using the synthetic solu-
 367 tion library, as well as the cost function are shown in Fig. 5. Compared to the other den-
 368 sity models considered, straightforward RBF yields the smallest MRE, thus it is the pre-
 369 ferred model to infer density in this work. However, the affine-transformed JLF method
 370 enables density inferences with accuracy comparable to those of more complex approaches.
 371 This simple and practical technique should be of interest in routine data analysis.

372 **3.2 Potential inference**

373 The floating potential of the spacecraft can also be inferred using the OML equa-
 374 tion, by rewriting equation 1 as:

$$375 \quad V_f \approx V_f + \frac{kT_e}{e} = \frac{V_2 I_1^{\frac{1}{\beta}} - V_1 I_2^{\frac{1}{\beta}}}{I_2^{\frac{1}{\beta}} - I_1^{\frac{1}{\beta}}} = \frac{V_3 I_2^{\frac{1}{\beta}} - V_2 I_3^{\frac{1}{\beta}}}{I_3^{\frac{1}{\beta}} - I_2^{\frac{1}{\beta}}}. \quad (14)$$

376 In this equation, the subscripts 1, 2, and 3 refer to different probes, thus there must be
 377 at least three probes in order to solve for β . The bias voltages of the probes and their
 378 corresponding collected currents are known from measurements, thus β can be solved
 379 using a standard root finder. Given β , equation 14 then provides a value for $V_f + \frac{kT_e}{e}$.
 380 In this expression, $\frac{kT_e}{e}$ is the electron temperature in electron-volt, which in the lower
 381 ionosphere at mid latitudes, is of order 0.3 eV or less. Thus, considering that $\frac{kT_e}{e}$ is gen-
 382 erally much smaller than satellite potentials relative to the background plasma, any of
 383 the two terms in the right side of Eq. 14 provide a first approximation of V_f (Guthrie
 384 et al., 2021). This will be referred to as the “corrected OML” approach. This equation
 385 works well when it is applied to the synthetic solution library with a MAE of 0.3 V cal-
 386 culated using currents collected with probe biases of 10, 9, and 8 volts probes. The er-
 387 ror of 0.3 V is likely due to the maximum electron temperature of 0.3 eV considered in
 388 the simulations. The β values calculated in the synthetic solution library is in the range
 389 of 0.75 to 1. It is also possible to build a model to infer floating potentials directly us-
 390 ing RBF regression. In this case, currents are normalized by dividing every current by

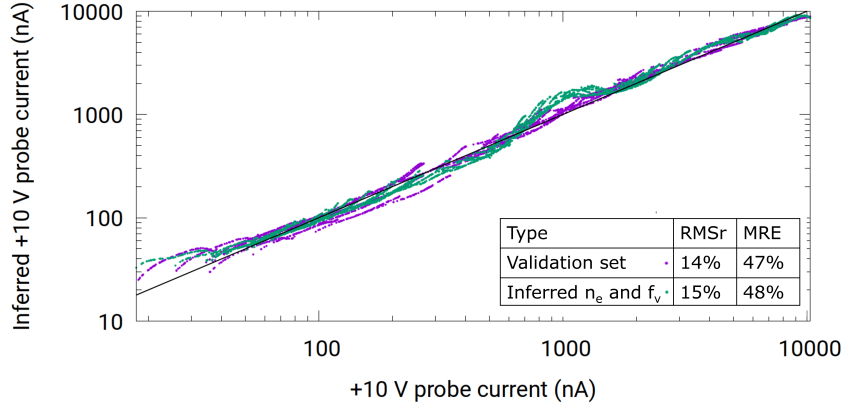


Figure 7. Correlation plot of inferred +10 V probe current against +10 V probe current from the synthetic data set is presented. The calculated +10 probe currents in purple curve is calculated using the validation data set, while the green curve is calculated using inferred densities and floating potentials from RBF regression.

391 their sum, in order to remove the strong density dependence on the currents. Using $G(x) =$
 392 $|x|$, and 5 centers, and minimizing MAE, the calculated MAE on the validation data set
 393 is 0.4 V. The inferred satellite potential from the BNLF approach has an RMS of 0.07
 394 V, and a MAE of 0.18 V, which proves this method to be the most accurate compared
 395 to the other methods considered. A correlation plot for potentials inferred using the RBF,
 396 corrected OML, and BNLF approaches is shown in Fig. 6. All methods show good agree-
 397 ment with values from the synthetic solution library.

398 3.3 Consistency check

399 In order to further assess the applicability of our inference approaches, we perform
 400 the following consistency check. First, RBF models $M1(n_e)$ and $M1(V_f)$ are constructed
 401 to infer the density and satellite potential using 4-tuple currents from our synthetic data
 402 set. A second model ($M2$) is constructed to infer collected currents from densities and
 403 floating potentials in our synthetic data set. Since we are not able to infer temperatures
 404 from the currents, the temperature is not included in $M2$. Consistency is then assessed
 405 in two steps, by i) using currents from synthetic data and models $M1(n_e)$ and $M1(V_f)$
 406 to infer densities and floating potentials, and ii) applying models $M2$ to these inferred
 407 values, to infer back collected currents. RBF density and floating potential inferences
 408 are used in $M1(n_e)$, and $M1(V_f)$ as described in sec. 3.1 and 3.2. RBF is also used in
 409 $M2$ with $G(x) = \sqrt{1 + x^{2.5}}$, and minimizing RMSr with 5 centers. With perfect infer-
 410 ence models, the results for these back-inferred currents, should agree exactly with the
 411 starting currents from synthetic data. Variances between back-inferred and simulated
 412 currents in the synthetic data are presented as indicative of the level of confidence in our
 413 regression techniques. The correlation plot in Fig. 7, shows back-inferred currents (green)
 414 calculated for a probe with 10 V bias against known currents from synthetic data. For
 415 comparison, the figure also shows the correlation between directly inferred currents (pur-
 416 ple) when model $M2$ is applied to densities and floating potentials in the synthetic data
 417 set. Both back-inferred and directly inferred currents are in excellent agreement with known
 418 currents from synthetic data, with comparable metric skills of $\simeq 15\%$ and $\simeq 48\%$ for
 419 the RMSr and the MRE, respectively. Considering that errors are compounded between
 420 the first and second models for the back-inferred currents, the nearly identical metric skills
 421 in Fig. 7 is seen as confirmation of the validity of our regression models.

4 Application to NorSat-1 data

In this section, we apply our density and potential inference models constructed with synthetic data, to in situ measurements made with the m-NLP on the NorSat-1 satellite. The NorSat-1 currents were obtained from a University of Oslo data portal (Hoang, Clausen, et al., 2018). The epoch considered corresponds to one and a half orbit of the satellite starting at approximately 10:00 UTC on January 4, 2020. We start with a comparison of simulated and measured currents to verify that our simulated currents are in the same range as those of measured in situ currents. Inferences made with RBF, neural network, BNLF, corrected OML, and the two corrected JLF approaches constructed in 3.1, are also presented.

4.1 Measured in-situ, and simulated currents

The relevance of the space plasma parameter range considered in the simulations, to NorSat-1, is assessed in Fig. 8, by plotting currents collected by the +9 V probe against that collected by the +10 V, from both synthetic data, and in situ measurements. The close overlap, and the fact that the range of in situ measurements is within the range of simulated currents, indicates that the physical parameters selected in the simulations, are indeed representative to conditions encountered along the NorSat-1 orbit.

The current measurement resolution for the NorSat-1 m-NLP probes is approximately 1 nA (Hoang, Clausen, et al., 2018). The noise level of the environment, however, is estimated to be of order 10 nA. In what follows, the darker color are used to represent inferences made using currents above 10 nA, and the lighter color are used to represent inferences using currents between 1 to 10 nA. This is done by filtering out all data that contain a current that is below 10 nA or 1 nA in any of the four probes. A word of caution is in order, however, for inferences made from these lower currents, as a conservative estimate of the threshold for sufficient signal-to-noise ratios, is approximately 10 nA. This lower bound current is supported by a consistency check made with models 1 and 2 described in Sec. 3.3, and presented below in Sec. 4.3.

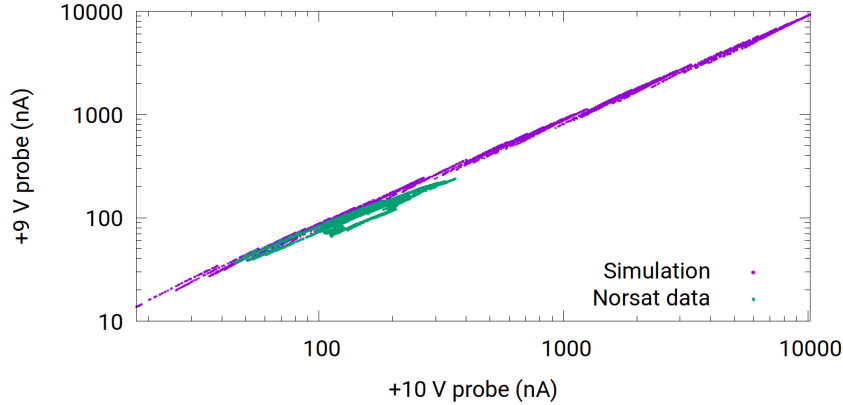


Figure 8. Correlation plot between currents collected by the +9 V and the +10 V probes for both NorSat-1, and synthetic data.

4.2 Density and satellite potential inference

Our models, trained with synthetic data as described in Sec. 3, are now applied to infer plasma densities and satellite potentials from in situ measured currents, for the

452 time period considered. The results obtained with the different models presented in Sec.
 453 3 are shown in Fig. 9 for the inferred densities, satellite potentials, and measured cur-
 454 rents collected by the four probes. The position of the satellite relative to the Earth and
 455 the Sun given by the solar zenith angle, is also plotted in the figure. For example, a small
 456 solar zenith angle means that the satellite is near the equator on the dayside.

457 Fitting the in-situ data with the BNLF method using the four measured currents
 458 is challenging. The +8 V probe currents are often slightly lower than expected for a down-
 459 ward concavity of I as a function of V_b , and tend to produce an upward concavity with
 460 β larger than 1. In this case, fitting the 4-tuples of currents using Eq. 1, for the density,
 461 the floating potential and β , with a specified electron temperature is not practical. Thus
 462 we used a fixed β value of 0.85, and fit only density and potential to the 4-tuples of cur-
 463 rents using Eq. 1. This choice for the value of β is justified by the fact that it produces
 464 the best inferences when applied to synthetic data, with an RMS error of 0.39 V for the
 465 floating potential, and an RMSr error of 27 % for the density. Based on comparisons made
 466 with our synthetic data sets, the use of a fixed β value results in a small loss in the in-
 467 ference accuracy for the satellite potential, but the accuracy of the inferred density is
 468 the same as when β is included as a third fitting parameter. Using the fixed values of
 469 0.172 eV for the electron temperature, and 0.85 for β , the RMSr error in the fits of the
 470 measured in situ currents, is 9%. The resulting inferred densities and satellite potentials
 471 are shown in Fig. 9. For reasons mentioned above, it is clear that no satellite potential
 472 below the fitting lower bound of -6 V can appear in the plot. On a practical note, an
 473 advantage of computing BNLF inferences with fixed temperature and β value, is that
 474 the nonlinear fit is made for only two fitting parameters (n_e and V_f), which results in
 475 faster convergence rates, compared to fits made with 4 or 3 adjustable parameters. In
 476 our calculations, for example, the convergence rate is 8 times faster with two, compared
 477 to three fitting parameters.

478 The densities shown in Fig. 9 panel b are obtained using the five density inference
 479 methods mentioned in Sec. 3.1. At 10:45, the neural network density, the RBF corrected
 480 JLF density, the RBF density, and the BNLF density ($\beta = 0.85$) overlap nicely, while
 481 the affine transformed JLF density is smaller than other inferred densities, particularly
 482 near the density maxima. The density inferences nonetheless qualitatively agree with each
 483 other. Using the +10, +9, and +8 NorSat-1 probe currents and Eq. 14, the inferred satel-
 484 lite floating potential is about -8 V for most of the data range considered in this study
 485 as shown in Fig. 9 panel c. This is in stark contradiction with observations in Fig. 9 panel
 486 d, which shows that the +6 V biased probe collects net positive electrons during most
 487 of the period considered. Also, there are periods between 10:15 to 10:30, and after 11:45
 488 when the + 6V probe collects ion current(negative), indicating drops in the satellite po-
 489 tential below -6 V. The poor performance of Eq. 14 to infer the satellite potential here,
 490 results from the fact that Eq. 14 yields erratic values of β ranging from 0.3 to 1.2. At-
 491 tempts have also been made to approximate the satellite potential with Eq. 14 using a
 492 fixed value of 0.58 and 0.78 for β , also resulting in satellite potentials in the -8 V range,
 493 and no improvement was found. This failure to produce acceptable values of the satel-
 494 lite potential clearly shows that this generalized OML approximation in Eq.14 does not
 495 provide a sufficiently accurate approximation for the currents collected by the NorSat-
 496 1 probes.

497 The RBF inferred floating potential shown in Fig. 9, is within -4 and -6 V, which
 498 is consistent with the observation that the +6 V probe collects electrons during most of
 499 the time period considered. Interestingly, the inferred satellite potential using currents
 500 between 1 and 10 nA (light color) is seen to join smoothly with the darker color infer-
 501 ences, and to decrease below -6 V around 10:25, which is consistent with the observa-
 502 tion that during that time the +6 V probe no longer collects electron current. The float-
 503 ing potentials inferred from the BNLF model are systematically lower than those from
 504 RBF, and they also fit within the acceptable range for the satellite potentials. The two
 505 potentials have otherwise a very similar time dependence. The +6 V probe collects zero
 506 net current near 10:25 in panel d. The BNLF potential is bounded by the fitting lower

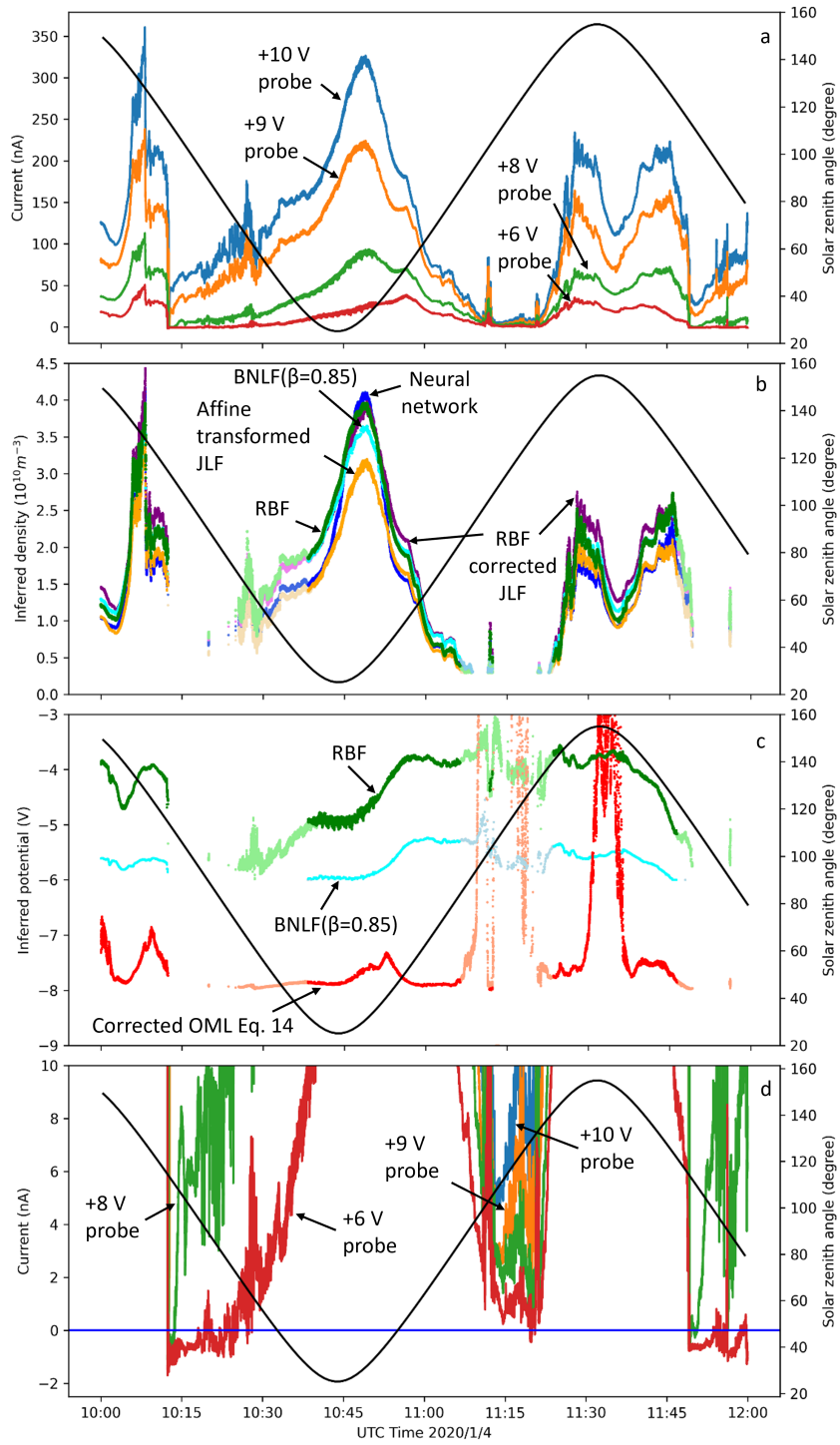


Figure 9. Illustrations of NorSat-1 collected currents considered in this study in panel a, inferred densities in panel b, inferred potentials in panel c, and the NorSat-1 current near 0 A in panel d. The solar zenith angle is also plotted against the secondary axis. Curves in darker colors are from model inferences using data above 10 nA, whereas those in lighter colors show inferences using data with currents between 1 nA and 10 nA.

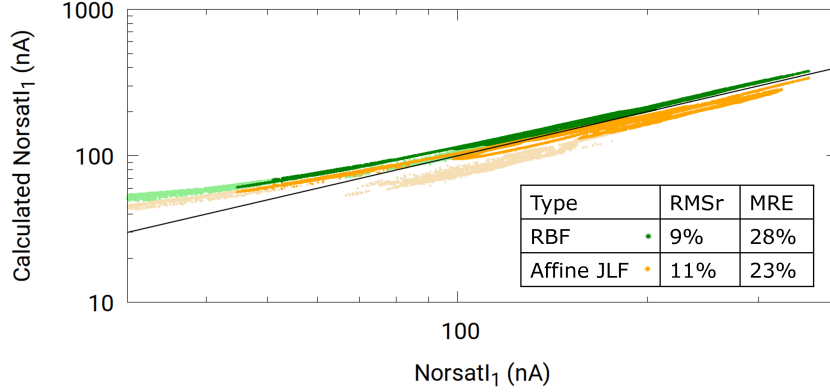


Figure 10. Consistency check is performed in the in situ data following the same procedure as in the synthetic data set. Both models 1 and 2 are trained with our synthetic data, and applied to currents from the +10 V probe on NorSat-1. Darker colors refer to inferences made with currents above 10 nA, while lighter colors refer to inferences obtained with currents between 1 and 10 nA.

507 limit of -6 V at these ranges, as opposed to RBF with which inferences are made with-
 508 out imposing an upper or lower bound. The currents collected by the probes are deter-
 509 mined mostly by the density and the satellite potential, and to a lesser extent, by the
 510 electron temperature. In Fig. 9, the density and floating potential are seen to peak at
 511 around 10:45 and 11:00 respectively. The currents from the +8, +9, and +10 V probes
 512 (green, orange, and blue) in panel a peak at around 10:45, coinciding with the peak in
 513 the plasma density at this time. Then, as time goes forward to 11:00, the currents of the
 514 three probes decrease, also coinciding with a decrease in plasma density. However, the
 515 +6 V probe (red) current is increasing during these times, possibly due to an increase
 516 in floating potential. This increase is captured in the RBF and BNLF inferred poten-
 517 tial, but not in the one derived from corrected OML. Another observation is that the in-
 518 ferred floating potential decreases significantly at 10:15, as the satellite crosses the ter-
 519 minator. On NorSat-1, the negative terminals of the solar cells are grounded to the space-
 520 craft bus while the positive side is facing the ambient plasma (Ivarsen et al., 2019). A
 521 likely explanation for the potential drop is that the solar cells facing the ambient plasma
 522 get charged positively and suddenly start collecting more electrons upon exiting solar
 523 eclipse. This would agree with findings reported by Ivarsen et al. (Ivarsen et al., 2019).

524 4.3 Consistency check

525 In the absence of accurate and validated inferred densities and satellite potentials
 526 from NorSat-1 data, it is not possible to confidently ascertain to what extent the infer-
 527 ences presented above are accurate. As an alternative, we proceed with a consistency check,
 528 following the same procedure as presented in Sec. 3.3 with synthetic data, but using mea-
 529 sured currents as input. This is done by first applying models $M1(n_e)$ and $M1(V_f)$ trained
 530 with synthetic data, to infer floating potentials and densities from measured currents.
 531 Then $M2$ (also trained with synthetic data) is used to infer currents from the $M1$ - in-
 532 ferred floating potentials and densities. If the models constructed from the synthetic data
 533 also apply to NorSat-1 data, the inferred currents should closely reproduce the measured
 534 NorSat-1 currents. A correlation plot of inferred against measured currents is shown in
 535 Fig. 10 for the +10 V probe. In this plot, the orange and green curves show back-inferred
 536 currents obtained with the RBF $M2$ model. For the orange curve (Affine JLF), the den-
 537 sity used as input in $M2$ is obtained with the affine transformed JLF method. For the

538 green curve (RBF), the density used as input in $M2$ is obtained with RBF density, while
 539 in both cases, the floating potentials are obtained with the $M1(V_f)$ model from RBF re-
 540 gression. The parts in lighter color are obtained using data with a 1nA filter, whereas
 541 the darker color parts are obtained using data with currents above 10 nA. While the graph
 542 only shows currents above 30 nA, the 1 nA filter curve extends to the left down to about
 543 5 nA, however, these calculated +10 volt probe currents plateau in this range and are
 544 far from the measured currents. This behavior is likely due to the noise level of the en-
 545 vironment which is about 10 nA, thus extra caution should be taken when using model
 546 inferences for data below 10 nA. The RMSr calculated for the 10 nA NorSat-1 current
 547 using direct RBF density as $M1(n_e)$ is 9%, and the MRE is 28 %, whereas these num-
 548 bers for the affine transformed JLF densities are 11 % and 23 %, respectively. The cal-
 549 culated +10 V probe current based on RBF regression and affine transformed JLF method
 550 nicely follows the measured +10 volt probe current except for a small increase in the vari-
 551 ance at lower currents, thus indicating that our model constructed with synthetic data
 552 set should be applicable to in situ data.

533 5 Conclusions

554 Two new approaches are presented and assessed, to infer plasma and satellite pa-
 555 rameters from currents measured with multiple fixed bias needle Langmuir probes. In
 556 the first approach, inferences are made with two multivariate regression techniques, con-
 557 sisting of radial basis functions, and neural networks. The second approach relies on a
 558 simple affine transformation combined with a technique first proposed by Jacobsen to
 559 infer the plasma density. Yet another approach, proposed by Barjatya, et al. is consid-
 560 ered, which consists of performing nonlinear fits of measured currents, to an analytic ex-
 561 pression involving the density, the floating potential and the exponent β as fitting pa-
 562 rameters, while the electron temperature is estimated by other means. In all cases, the
 563 accuracy of inferences is assessed on the basis of synthetic data obtained from kinetic
 564 simulations made for space-plasma conditions representative of those encountered along
 565 the NorSat-1 satellite. In addition to assessments based on synthetic data, a consistency
 566 check is presented, whereby densities and satellite potentials inferred from collected cur-
 567 rents, are used as input in an inverse regression model to infer currents for one of the
 568 probes. The advantage of this consistency check is that it is applicable to both synthetic,
 569 and in situ measured currents, and in the latter case, it does not rely on a priori given
 570 inferred densities and satellite potentials. Inference consistency checks are made with
 571 both synthetic and in situ measured currents, showing excellent agreement.

572 The density inference methods considered in this study yield excellent results when
 573 applied to the synthetic data set. The models constructed with synthetic data are then
 574 applied to currents measured by the four m-NLP on NorSat-1. When applied to NorSat-
 575 1 data, the Barjatya nonlinear fit approach is modified by assuming a fixed value for β ,
 576 and carrying the fit with only the electron density and satellite potential as fitting pa-
 577 rameters. The density inferences from all methods show good agreement, which suggests
 578 that either method should be a significant improvement over the commonly used OML
 579 approach based on $\beta = 0.5$. From our findings, direct RBF and the combination of
 580 Jacobsen's linear fit with $\beta = 0.5$ with an affine transformation, appear as being the
 581 most promising, and deserving of further study. These two methods provide inferences
 582 that are consistent and quantitatively similar, while being relatively simple and numer-
 583 ically efficient. The former yields the lowest maximum relative error when assessed with
 584 synthetic data, whereas the latter is the simplest method and produces inferences with
 585 comparable accuracy. The spacecraft floating potential is also inferred using RBF regres-
 586 sion, a modified OML approach and Barjatya nonlinear fit method. The modified OML
 587 inferences are inconsistent with the measurements from NorSat-1 data since it indicates
 588 that the satellite potential is below -6V, while measurements indicate that the +6 V probe
 589 is collecting electron current. Conversely, spacecraft potentials inferred with RBF regres-
 590 sion, and the nonlinear fit approach yield potentials that are consistent with measured

591 currents from the +6 V biased probe, showing that the satellite potential must have been
 592 at or above -6 V for most of the one and a half orbital period considered. This failure
 593 to produce acceptable values of the satellite potential using Eq. 14, and the fact that the
 594 Barjatya nonlinear fit approach with n_e , V_f , and β as fitting parameters, results in β val-
 595 ues appreciably larger than one, shows that in situ measurements on NorSat-1 generally
 596 do not follow the empirical expression in Eq. 1.

597 The analysis presented here has been focused on fixed bias multi-needle Langmuir
 598 probes, with the same dimensions as the ones mounted on NorSat-1, to which it has been
 599 applied as a case study. We stress, however, that the simulation-regression approach to
 600 infer space plasma parameters, is not limited to fixed bias probes or to this particular
 601 configuration of probes. With kinetic solutions capable of reproducing analytic results
 602 in conditions when they are valid, and also capable of accounting for more physics, and
 603 more realistic geometries than theories, solution libraries, training and validation sets
 604 can just as well be constructed for different probes, mounted on satellites, operated in
 605 fixed or sweep bias voltage mode. By following standard machine learning procedures,
 606 whereby models are trained on a subset of a solution library of known independent and
 607 dependent variables, and tested by applying them to distinct subsets, we can estimate
 608 uncertainty margins specifically associated with different inference techniques. Another
 609 important strength of the proposed simulation-regression approach is that it enables rel-
 610 atively straightforward incremental improvements to a model, by accounting for more
 611 physical processes or more detailed geometries; something that would be very difficult
 612 to do in a theory. Implementation of regression models and affine transformation of the
 613 linear fit model involves simple arithmetic expressions with pre-calculated coefficients
 614 and can easily be programmed for onboard processing of low level data. These approaches,
 615 however, would require the creation of custom data sets, when applied to a given mis-
 616 sion, so as to account for the geometry relevant to the measuring instruments, and the
 617 space environment conditions expected along a satellite orbit. This is where the BNLF
 618 technique could prove convenient, as it does not rely on the construction of extensive syn-
 619 thetic data sets and training strategies. This approach does, however, require more com-
 620 putational resources, which would necessitate optimization in order to be implemented
 621 onboard a satellite. The work presented here is by no means final. The development of
 622 improved inference approaches based on simulations and regression techniques will re-
 623 quire significantly more efforts, involving collaborations between experimentalists and
 624 modelers; an effort well worth doing, considering the cost and years of preparation in-
 625 volved in scientific space missions.

626 Acknowledgments

627 This work was supported by the China Scholarship Council, the Natural Sciences and
 628 Engineering Research Council of Canada, the Research Council of Norway (Grant Agree-
 629 ment No. 275655 and 325074), and the European Research Council (ERC) under the Eu-
 630 ropean Union’s Horizon 2020 research and innovation program (Grant Agreement No.
 631 866357, POLAR-4DSpace). The kinetic simulations used in this study were made on the
 632 Compute Canada computing infrastructure. S.M. also acknowledges Dag Mortensen, Øyvind
 633 Jensen, and the Institute for Energy Technology for permission to participate in this re-
 634 search.

635 References

- 636 Abadi, M., Barham, P., Chen, J., Chen, Z., Davis, A., Dean, J., ... others (2016).
 637 Tensorflow: A system for large-scale machine learning. In (p. 265-283).
 638 Allen, J. E., Boyd, R. L. F., & Reynolds, P. (1957, 3). The collection of positive ions
 639 by a probe immersed in a plasma. *Proceedings of the Physical Society. Section*
 640 *B*, 70, 297-304. Retrieved from [https://doi.org/10.1088/0370-1301/70/](https://doi.org/10.1088/0370-1301/70/3/303)
 641 [3/303https://iopscience.iop.org/article/10.1088/0370-1301/70/3/303](https://iopscience.iop.org/article/10.1088/0370-1301/70/3/303)

- doi: 10.1088/0370-1301/70/3/303
- 642 Barjatya, A., & Merritt, W. (2018). Error analysis of multi-needle langmuir probe
643 measurement technique. *Review of Scientific Instruments*, 89, 1-5. Retrieved
644 from <http://dx.doi.org/10.1063/1.5022820> doi: 10.1063/1.5022820
- 645 Barjatya, A., St-Maurice, J. P., & Swenson, C. M. (2013). Elevated electron
646 temperatures around twin sporadic e layers at low latitude: Observations
647 and the case for a plausible link to currents parallel to the geomagnetic
648 field. *Journal of Geophysical Research: Space Physics*, 118, 7316-7328. doi:
649 10.1002/2013JA018788
- 650 Barjatya, A., Swenson, C. M., Thompson, D. C., & Wright, K. H. (2009). In-
651 vited article: Data analysis of the floating potential measurement unit aboard
652 the international space station. *Review of Scientific Instruments*, 80. doi:
653 10.1063/1.3116085
- 654 Bekkeng, T. A., Jacobsen, K. S., Bekkeng, J. K., Pedersen, A., Lindem, T., Lebre-
655 ton, J. P., & Moen, J. I. (2010, 8). Design of a multi-needle langmuir probe
656 system. *Measurement Science and Technology*, 21, 085903. Retrieved from
657 <https://iopscience.iop.org/article/10.1088/0957-0233/21/8/085903>
658 doi: 10.1088/0957-0233/21/8/085903
- 659 Bernstein, I. B., & Rabinowitz, I. N. (1959). Theory of electrostatic probes in a
660 low-density plasma. *Physics of Fluids*, 2, 112. Retrieved from [https://aip](https://aip.scitation.org/doi/10.1063/1.1705900)
661 [.scitation.org/doi/10.1063/1.1705900](https://aip.scitation.org/doi/10.1063/1.1705900) doi: 10.1063/1.1705900
- 662 Bhattarai, S., & Mishra, L. N. (2017, 8). Theoretical study of spherical langmuir
663 probe in maxwellian plasma. *International Journal of Physics*, 5, 73-81.
664 Retrieved from <http://pubs.sciepub.com/ijp/5/3/2/index.html> doi:
665 10.12691/ijp-5-3-2
- 666 Bilitza, D., Altadill, D., Zhang, Y., Mertens, C., Truhlik, V., Richards, P., ...
667 Reinisch, B. (2014, 2). The international reference ionosphere 2012 – a model
668 of international collaboration. *Journal of Space Weather and Space Climate*, 4,
669 A07. Retrieved from <http://www.swsc-journal.org/10.1051/swsc/2014004>
670 doi: 10.1051/swsc/2014004
- 671 Chalaturnyk, J., & Marchand, R. (2019, 5). Regression-based interpretation of
672 langmuir probe measurements. *Frontiers in Physics*, 7. Retrieved from
673 <https://www.frontiersin.org/article/10.3389/fphy.2019.00063/full>
674 doi: 10.3389/fphy.2019.00063
- 675 Chen, F. F. (1965, 1). Numerical computations for ion probe characteristics in
676 a collisionless plasma. *Journal of Nuclear Energy. Part C, Plasma Physics,*
677 *Accelerators, Thermonuclear Research*, 7, 47-67. Retrieved from [https://](https://doi.org/10.1088/0368-3281/7/1/306)
678 doi.org/10.1088/0368-3281/7/1/306[https://iopscience.iop.org/](https://iopscience.iop.org/article/10.1088/0368-3281/7/1/306)
679 [article/10.1088/0368-3281/7/1/306](https://iopscience.iop.org/article/10.1088/0368-3281/7/1/306) doi: 10.1088/0368-3281/7/1/306
- 680 Chen, F. F. (2003). Lecture notes on langmuir probe diagnostics. Mini-Course on
681 Plasma Diagnostics, IEEEICOPS meeting. Retrieved from [http://www.seas](http://www.seas.ucla.edu/~ffchen/Publs/Chen210R.pdf)
682 [.ucla.edu/~ffchen/Publs/Chen210R.pdf](http://www.seas.ucla.edu/~ffchen/Publs/Chen210R.pdf)
- 683 Debchoudhury, S., Barjatya, A., Minow, J. I., Coffey, V. N., & Chandler, M. O.
684 (2021, 10). Observations and validation of plasma density, tempera-
685 ture, and o+ abundance from a langmuir probe onboard the international
686 space station. *Journal of Geophysical Research: Space Physics*, 126. doi:
687 10.1029/2021JA029393
- 688 Ergun, R. E., Andersson, L. A., Fowler, C. M., & Thaller, S. A. (2021, 3). Kinetic
689 modeling of langmuir probes in space and application to the MAVEN langmuir
690 probe and waves instrument. *Journal of Geophysical Research: Space Physics*,
691 126. doi: 10.1029/2020JA028956
- 692 Frey, P., & George, P. L. (2007). *Mesh generation: Application to finite elements*.
693 ISTE.
- 694 Geuzaine, C., & Remacle, J.-F. (2009, 9). Gmsh: A 3-D finite element mesh gener-
695 ator with built-in pre- and post-processing facilities. *International Journal for*
696

- 697 *Numerical Methods in Engineering*, 79, 1309-1331. Retrieved from [http://doi](http://doi.wiley.com/10.1002/nme.2579)
698 [.wiley.com/10.1002/nme.2579](http://doi.wiley.com/10.1002/nme.2579) doi: 10.1002/nme.2579
- 699 Goodfellow, I., Bengio, Y., & Courville, A. (2016). *Deep learning*. MIT Press. Re-
700 trieved from <https://books.google.ca/books?id=Np9SDQAAQBAJ>
- 701 Guthrie, J., Marchand, R., & Marholm, S. (2021). Inference of plasma parameters
702 from fixed-bias multi-needle langmuir probes (m-NLP). *Measurement Science*
703 *and Technology*, 32. doi: 10.1088/1361-6501/abf804
- 704 Hoang, H., Clausen, L. B., Røed, K., Bekkeng, T. A., Trondsen, E., Lybekk, B.,
705 ... Moen, J. I. (2018, 6). The multi-needle langmuir probe system on
706 board NorSat-1. *Space Science Reviews*, 214, 75. Retrieved from [http://](http://dx.doi.org/10.1007/s11214-018-0509-2)
707 dx.doi.org/10.1007/s11214-018-0509-2
708 [http://link.springer.com/](http://link.springer.com/10.1007/s11214-018-0509-2)
10.1007/s11214-018-0509-2 doi: 10.1007/s11214-018-0509-2
- 709 Hoang, H., Røed, K., Bekkeng, T. A., Moen, J. I., Clausen, L. B., Trondsen, E., ...
710 Sagi, E. (2019). The multi-needle langmuir probe instrument for QB50 mis-
711 sion: Case studies of Ex-Alta 1 and hoopoe satellites. *Space Science Reviews*,
712 215. Retrieved from <http://dx.doi.org/10.1007/s11214-019-0586-x> doi:
713 10.1007/s11214-019-0586-x
- 714 Hoang, H., Røed, K., Bekkeng, T. A., Moen, J. I., Spicher, A., Clausen, L. B. N.,
715 ... Pedersen, A. (2018, 6). A study of data analysis techniques for the multi-
716 needle langmuir probe. *Measurement Science and Technology*, 29, 065906.
717 Retrieved from [https://iopscience.iop.org/article/10.1088/1361-6501/](https://iopscience.iop.org/article/10.1088/1361-6501/aab948)
718 [aab948](https://iopscience.iop.org/article/10.1088/1361-6501/aab948) doi: 10.1088/1361-6501/aab948
- 719 Hoskinson, A. R., & Hershkowitz, N. (2006). Effect of finite length on the
720 current-voltage characteristic of a cylindrical langmuir probe in a multidipole
721 plasma chamber. *Plasma Sources Science and Technology*, 15, 85-90. doi:
722 10.1088/0963-0252/15/1/013
- 723 Ivarsen, M. F., Hoang, H., Yang, L., Clausen, L. B., Spicher, A., Jin, Y., ... Lybekk,
724 B. (2019). Multineedle langmuir probe operation and acute probe current
725 susceptibility to spacecraft potential. *IEEE Transactions on Plasma Science*,
726 47, 3816-3823. doi: 10.1109/TPS.2019.2906377
- 727 Jacobsen, K. S., Pedersen, A., Moen, J. I., & Bekkeng, T. A. (2010). A new lang-
728 muir probe concept for rapid sampling of space plasma electron density. *Mea-*
729 *surement Science and Technology*, 21. doi: 10.1088/0957-0233/21/8/085902
- 730 Johnson, J. D., & Holmes, A. J. T. (1990, 10). Edge effect correction for small plan-
731 nar langmuir probes. *Review of Scientific Instruments*, 61, 2628-2631. doi: 10
732 .1063/1.1141849
- 733 Kingma, D. P., & Ba, J. (2015). Adam: A method for stochastic optimization. In
734 Y. Bengio & Y. LeCun (Eds.), . Retrieved from [http://arxiv.org/abs/1412](http://arxiv.org/abs/1412.6980)
735 [.6980](http://arxiv.org/abs/1412.6980)
- 736 Laframboise, J. G. (1966). Theory of spherical and cylindrical langmuir probes in
737 a collisionless, maxwellian plasma at rest. *Toronto Univ. (Ontario). Inst. for*
738 *Aerospace Studies*. Retrieved from <https://www.osti.gov/biblio/4522330>
- 739 Lebreton, J.-P., Stverak, S., Travnicsek, P., Maksimovic, M., Klinge, D., Merikallio,
740 S., ... Salaquarda, M. (2006, 4). The ISL langmuir probe experiment
741 processing onboard DEMETER: Scientific objectives, description and
742 first results. *Planetary and Space Science*, 54, 472-486. Retrieved from
743 <https://linkinghub.elsevier.com/retrieve/pii/S0032063305002084>
744 doi: 10.1016/j.pss.2005.10.017
- 745 Lira, P. A. R., Marchand, R., Burchill, J., & Forster, M. (2019, 8). Deter-
746 mination of Swarm front plate's effective cross section from kinetic sim-
747 ulations. *IEEE Transactions on Plasma Science*, 47, 3667-3672. Re-
748 trieved from <https://ieeexplore.ieee.org/document/8725927/> doi:
749 10.1109/TPS.2019.2915216
- 750 Liu, G., & Marchand, R. (2021). Kinetic simulation of segmented plasma flow me-
751 ter response in the ionospheric plasma. *Journal of Geophysical Research: Space*

- 752 *Physics*, 126. doi: 10.1029/2021JA029120
- 753 Marchand, R. (2012, 2). PTetra, a tool to simulate low orbit satellite–plasma inter-
 754 action. *IEEE Transactions on Plasma Science*, 40, 217-229. Retrieved from
 755 <http://ieeexplore.ieee.org/document/6069605/> doi: 10.1109/TPS.2011
 756 .2172638
- 757 Marchand, R., & Lira, P. A. R. (2017, 4). Kinetic simulation of space-
 758 craft–environment interaction. *IEEE Transactions on Plasma Science*, 45,
 759 535-554. Retrieved from <http://ieeexplore.ieee.org/document/7888602/>
 760 doi: 10.1109/TPS.2017.2682229
- 761 Marholm, S., & Marchand, R. (2020, 4). Finite-length effects on cylindrical
 762 langmuir probes. *Physical Review Research*, 2, 023016. Retrieved from
 763 <https://link.aps.org/doi/10.1103/PhysRevResearch.2.023016> doi:
 764 10.1103/physrevresearch.2.023016
- 765 Marholm, S., Marchand, R., Darian, D., Miloch, W. J., & Mortensen, M. (2019,
 766 8). Impact of miniaturized fixed-bias multineedle langmuir probes on
 767 CubeSats. *IEEE Transactions on Plasma Science*, 47, 3658-3666. Re-
 768 trieved from <https://ieeexplore.ieee.org/document/8734022/> doi:
 769 10.1109/TPS.2019.2915810
- 770 Mott-Smith, H. M., & Langmuir, I. (1926). The theory of collectors in gaseous dis-
 771 charges. *Physical Review*, 28, 727-763. doi: 10.1103/PhysRev.28.727
- 772 Olowookere, A., & Marchand, R. (2021). Fixed bias probe measurement of a satellite
 773 floating potential. *IEEE Transactions on Plasma Science*, 49, 862-870. doi: 10
 774 .1109/TPS.2020.3045366
- 775 Rudakov, D. L., Boedo, J. A., Moyer, R. A., Lehmer, R. D., Gunner, G., & Watkins,
 776 J. G. (2001). Fast electron temperature diagnostic based on langmuir probe
 777 current harmonic detection on DIII-D. *Review of Scientific Instruments*, 72,
 778 453-456. doi: 10.1063/1.1310577
- 779 Saad, Y. (2003). *Iterative methods for sparse linear systems* (Second ed.). Society
 780 for Industrial and Applied Mathematics. Retrieved from [https://epubs.siam](https://epubs.siam.org/doi/abs/10.1137/1.9780898718003)
 781 [http://epubs.siam.org/doi/](http://epubs.siam.org/doi/book/10.1137/1.9780898718003)
 782 [book/10.1137/1.9780898718003](http://epubs.siam.org/doi/book/10.1137/1.9780898718003) doi: 10.1137/1.9780898718003
- 783 Sheridan, T. E. (2010, 3). The plasma sheath around large discs and ion collection
 784 by planar langmuir probes. *Journal of Physics D: Applied Physics*, 43, 105204.
 785 doi: 10.1088/0022-3727/43/10/105204
- 786 Sudit, I. D., & Woods, R. C. (1994). A study of the accuracy of various langmuir
 787 probe theories. *Journal of Applied Physics*, 76, 4488-4498. doi: 10.1063/1
 788 .357280